Nanomechanical properties of Au (111), (001), and (110) surfaces

J. D. Kiely and J. E. Houston
Surface and Interface Sciences Department, Sandia National Laboratories, Albuquerque, New Mexico 87185-1413
(Received 22 December 1997)

Using the interfacial force microscope in an indentation mode, we have quantitatively investigated the mechanical properties for the (111), (001), and (110) surfaces of Au single crystals. Nanoscale indentations of wide, atomically flat terraces provide a measure of the nanomechanical properties of Au in the absence of bulk and surface defects. The elastic indentation modulus for the (111) surface was found to be 36% greater than for the (001) and 3% greater than for the (110) surfaces. These results are compared to earlier theoretical predictions of the effect of anisotropy on indentation based on continuum mechanics and atomistic simulations. Additionally, we have quantified the yield point of the three crystal orientations by measuring the stress at which initial plastic deformation occurs. By resolving the applied stresses on {111} slip planes, we have estimated maximum shear stresses at the yield point. For each orientation, plastic deformation occurred when the maximum resolved shear stress reached approximately 1.8 GPa on all {111} planes that appeared to contribute to deformation. Based on this estimate, we propose that the critical resolved shear stress for plastic indentation of Au is 1.8 GPa and that the yield criterion is that this stress be attained on all {111} slip planes noncoplanar with the surface. [S0163-1829(98)06319-X]

INTRODUCTION

Nanoscale material properties have received considerable interest in recent years because small volumes often behave differently than do their macroscopic counterparts and, in some cases, approach theoretical limits.[1–7] Understanding the mechanical properties of small volumes has been motivated by the development of thin film and nanostructured materials. One class of techniques well-suited to investigate these properties is nanoscale scanning-probe indentation,[8–11] where the volume of the material probed is determined by the radius of the probe and the depth of deformation. Recently, the yield strength or hardness of materials has been shown to be dependent upon these two experimental parameters,[1,12] clearly indicating that these properties change with sampling volume.

One complicating factor in nanoindentation measurements is the effect of anisotropy. Nearly all metals are to some degree elastically anisotropic, and when the volume being probed by a nanoscale indentation is smaller than the grain size, properties of single crystals are being measured. In the present paper, we investigate the effect of anisotropy using the interfacial force microscope (IFM) (Ref. 13) in a nanoindentation mode. We study Au, one of the most anisotropic metals, and investigate the (111), (110), and (001) surfaces of carefully prepared single crystals. Two key elements of these studies are that the surfaces were passivated to eliminate tip-sample adhesive effects and had terraces wider than $\sim$4000 Å. We tabulate the indentation modulus and the maximum shear stress at the onset of plastic deformation, compare them with other experimental results, and develop a simple model for the critical shear stress for creating a permanent indentation.

EXPERIMENTAL PROCEDURES

Mechanical measurements were performed using the IFM. This instrument, which has been described in detail elsewhere,[13] is distinguished by its use of a novel electrostatically driven force-feedback system to ensure rigid displacement control during a loading experiment. Rigid displacement control ensures that instrument compliance (common in many indentation studies) does not exist, which simplifies analysis of elastic force profiles. Rigid displacement control is also advantageous when investigating the process by which materials plastically deform. Instabilities (e.g., jump-to-contact) are not present in this instrument and no energy is released from the sensor when a material's relaxation is plastic.

The IFM force sensor was calibrated prior to use, as were the piezoactuators used in the loading cycle. Both calibrations are necessary for quantitative measurements. The two indenters used in this study were electrochemically etched 100 μm tungsten wires with measured tip radii of 1750 and 700 Å, as determined by field-emission scanning electron microscopy. Single-crystal Au samples with (001) and (110) surface orientations were Ar-ion sputtered and annealed at 950 °C. The (111) surfaces were obtained by flame melting and annealing 99.99% pure Au wire to form a sphere with broad (111) facets[14,15] Immediately after cleaning, samples were immersed in a 0.5 mM ethanolic alkanethiol $[CH_3(CH_2)_{15}SH]$ solution for 24 h to develop a self-assembled monolayer (SAM) of hexadecanethiol to passivate the probe-sample interaction. Without the SAM, strong adhesive interaction occurs between the Au and W tip and the material is plastic on contact.[4,16] Passivation eliminates this adhesion[4,17] and allows us to analyze elastic force profiles using Hertzian theory,[18,19] which predicts the elastic behavior of a parabolic tip and planar sample in the absence of adhesive or frictional interactions using continuum elasticity.

A typical force profile for a 700 Å tip is shown in Fig. 1. The positive force axis refers to repulsive forces and the position is referenced to the point of contact, which is loosely identified as the point at which the measured force starts to rise from zero. Negative deformation values indicate

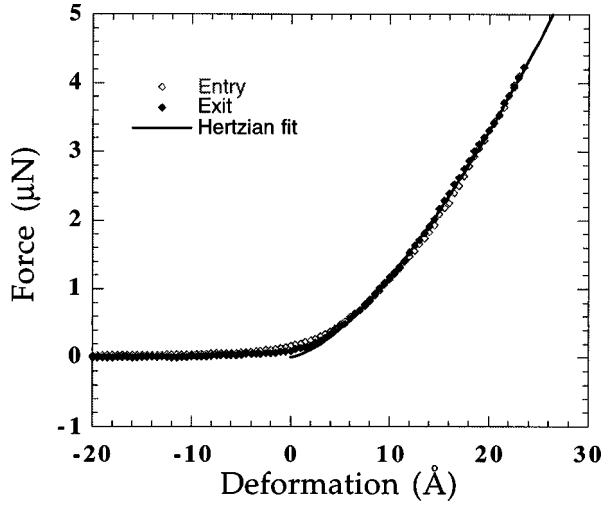

FIG. 1. A force profile (loading cycle) for a 700 Å W tip contacting a Au (111) surface. After contact, the force increases as the 3/2 power of the deformation, in accordance with the Hertzian relationship, shown as the solid line. The absence of hysteresis indicates elastic loading, and the absence of negative forces shows that there were virtually no adhesive forces throughout the experiment.

that the tip and sample are not in contact and zero force is measured. The small positive forces near the point of contact in Fig. 1 correspond to compression of the SAM, which initially dominates the force response. As the sample is deformed, the force rises nonlinearly to a preset maximum of 4.5 μN and this behavior is retraced upon retraction. The absence of a hysteresis loop during this measurement cycle indicates that the sample was probed elastically, and the absence of any attractive forces shows that there were virtually no adhesive forces throughout the experiment. The data may be fit using the expected Hertzian response for a parabaloid indenting a plane, as shown by the solid line in Fig. 1. The Hertzian response is given by the expression[19]

$$F = \tfrac{4}{3} E^* \sqrt{R}\, \delta^{3/2}, \tag{1}$$

where F is the force applied to the probe, R is the probe radius, δ is the depth of deformation, and E^* is the composite modulus, given by

$$\frac{1}{E^*} = \frac{(1-\nu_{\mathrm{Au}}^2)}{E_{\mathrm{Au}}} + \frac{(1-\nu_{\mathrm{W}}^2)}{E_{\mathrm{W}}}, \tag{2}$$

where E_{Au}, E_{W}, ν_{Au}, and ν_{W} refer to the elastic modulus and Poisson ratios of Au and W. The Hertzian model was developed for isotropic materials and, although Au has a high degree of anisotropy in elastic constants, elastic force profiles [both measured experimentally and modeled using embedded atom method (EAM) calculations[20]] show very good agreement with Hertzian predictions.

RESULTS

Elastic modulus

To identify the effect of crystal orientation on the measured indentation modulus, a single probe and sensor were used to acquire a series of force profiles from flat, defect-free regions of (111) and (001) orientations. Using a different

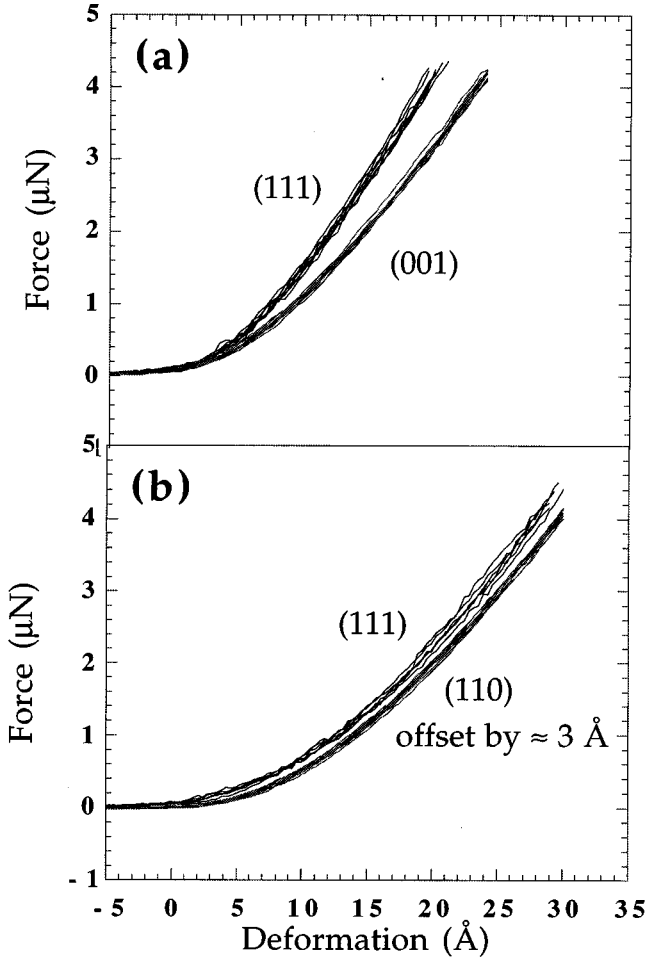

FIG. 2. (a) Compiled retraction portion of loading cycles from (111)-oriented and (001)-oriented surfaces. The greater slope of the (111) force profiles indicates a higher indentation modulus. (b) Compiled retraction portion of loading cycles for (111)-oriented and (110)-oriented surfaces. The (110) force profiles have been offset by approximately 3 Å to distinguish the two data sets. The lack of any noticeable difference in the slopes indicates a difference in indentation modulus that is on the order of the scatter in measurement.

probe, this was repeated for (111) and (110) orientations such that the response of the (111) acted as the reference. Ten loading cycles acquired in different locations were analyzed from each surface. The retraction portion of the loading cycles for the (111)-(001) comparison are shown in Fig. 2(a). Similar results from (111) and (110) orientations are shown in Fig. 2(b), although the data from the (110) have been offset by several angstroms to distinguish the two groupings.

To quantify the measured modulus, we fit Eq. (1) to each force profile with the composite modulus as the only independent variable. The composite moduli were averaged and this average was reduced to the Au modulus using Eq. (2) and a value of 411 GPa for the W modulus. The ratio of the s_{13} term to the s_{33} term in the orientation-specific compliance matrix was used as the Poisson's ratio, which, for the (111) and (001) directions, has values of 0.44 and 0.46.[21] In the (110)-orientation compliance matrix $s_{13} \neq s_{23}$, but for simplicity, the two ratios were averaged to give $\nu = 0.45$. The results for the elastic modulus measurements are shown in

TABLE I. Composite moduli and Au indentation moduli measured from force profiles during retraction on Au (111), (001), and (110) surfaces. Two comparative experiments were performed using different tip-sensor combinations, resulting in different (111) moduli. Experimental uncertainty is that within one experiment (same tip and sensor).

	E^* (GPa)	E_{Au} (GPa)
(111)	79±1	78±1
(001)	62±4	57±3
(111)	85±7	85±7
(110)	83±7	82±6

Table I, along with the experimental uncertainties, which represents scatter among measurement cycles using the same tip-sample combination. Taking the ratio of measurements from two orientations eliminates systematic errors, such as an error in tip radius estimate, that result in variation between experiments. For example, an overestimation in tip radius of only 10% accounts for the difference in measured (111) moduli between experiments. From these measurements, the elastic indentation modulus of Au oriented with a (111) surface normal is approximately 36% higher than Au with a (001) surface normal. Also, there appears to be no statistically significant difference in the elastic indentation moduli of Au crystals with (111) and (110) orientations.

Plastic yield

In addition to elastic properties, the stress required for plastic deformation was also measured as a function of orientation. Deviation from Hertzian behavior identifies the onset of plastic deformation. In some cases, this deviation was slight, but still identifiable, while in many cases, an abrupt and significant decrease in force identified the onset of plasticity. As an example of this abrupt onset of dislocation activity, Fig. 3 presents the response of a Au (001) crystal. Over the first 40–50 Å of deformation, the Au behaves elastically and, if the probe were to be removed, the force would decrease according to the Hertzian prediction. At a depth of approximately 50 Å and a force of approximately 14.5 μN, the measured force suddenly drops to 5 μN. As the probe continues to indent the sample, the force rises and drops as dislocation activity continues. From the force (F), depth of deformation (δ), and tip radius (R), the mean applied stress normal to the surface at the initiation of dislocation activity may be calculated from the expression[18]

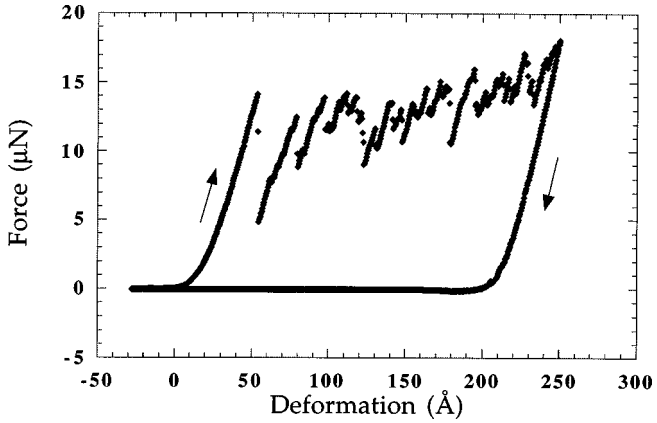

FIG. 3. Loading cycle of a (111)-oriented surface when the elastic limit is surpassed. The initial ~50 Å of deformation is elastic and deviation from this Hertzian behavior identifies the initial yield point. Sudden force drops indicate dislocation activity, which continues until the probe is retracted. The width of the hysteresis loop, approximately 200 Å in this case, indicates the depth of the permanent indentation.

TABLE II. Mean stress normal to the surface at the first deviation from Hertzian behavior.

Orientation	$\overline{\sigma_p}$ (GPa)
(001)	5.5±0.4
(111)	7.3±0.5
(110)	7.8±0.7

$$\overline{\sigma_p}=\frac{F_t}{\pi R\,\delta_t}, \tag{3}$$

where the subscript indicates the value at the plastic threshold. The mean plastic-threshold stress, whether it was in the form of a sudden drop in force or a more subtle deviation from elastic behavior, was found to be strongly dependent upon crystal orientation. The results are presented in Table II.

Indentation symmetry

Orientation not only affected the yield point, it also affected the symmetry of plastic indentations. Permanent indentations with depths of approximately 200 Å for each of the three sample orientations are presented as constant repulsive-force images in Fig. 4. As shown in Fig. 5(a) (111) planes, the dominant slip planes in this material, intersect the (001) surface with fourfold symmetry and this is observed in the permanent indentation. Additionally, the pileup on the indentation periphery (which was no greater than ~10 Å in height) appears to be in four distinct lobes. (111) planes intersect the (111) surface with threefold symmetry and the observed indentation from the (111) surface has the expected triangular appearance. For the (110) surface, (111) planes intersect the surface along three directions and the indentation from this surface has a roughly hexagonal appearance. The corners of the indentation do not exactly match the expected angles, but it is clear that the underlying crystallography plays a large role in determining the shape of the permanent indentation. The observed indentation symmetries are consistent with theoretical models of plastic deformation of Au surfaces under an indenter.[20]

DISCUSSION

Elastic modulus

The strong effect of crystal orientation on both the elastic modulus and the yield stress indicates that anisotropic effects play a significant role in nanoindentation. Our results suggest that anisotropy has a 30–40 % effect on the indentation

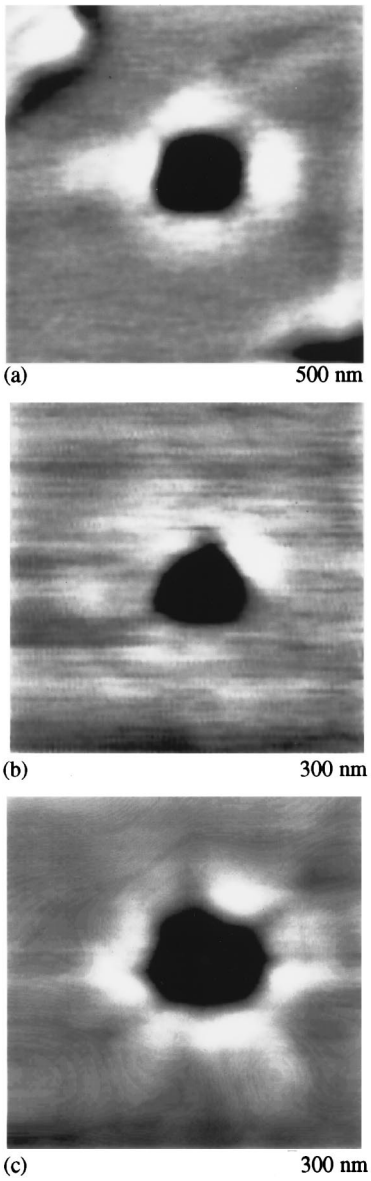

FIG. 4. (a) Constant repulsive-force image (500×500 nm^2) of a permanent indentation on a (001)-oriented surface. The fourfold shape of the indentation and the four lobes of pileup on the indentation periphery indicate the fourfold intersection of (111) slip planes with the surface. (b) A 300×300 nm^2 image of a permanent indentation on a (111)-oriented surface. The triangular appearance of the indentation reveals the threefold intersection of (111) slip planes with the surface. (c) A 300×300 nm^2 image of a permanent indentation on a (110)-oriented surface. The indentation symmetry suggests that the orientation of (111) slip planes determines the structure of both the indentation and surrounding pileup.

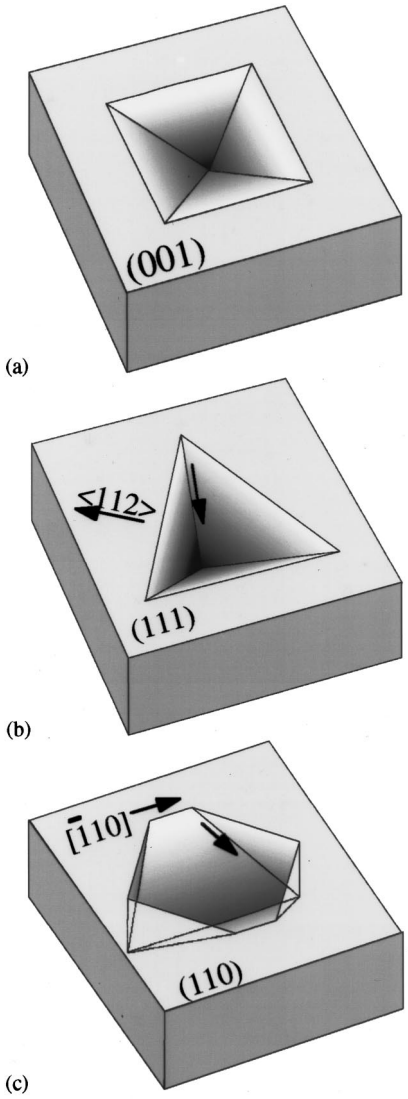

FIG. 5. (a) Schematic illustration of the four {111} planes that intersect the (001) surface. Slip occurs on these planes along the ⟨110⟩ directions, each of which is parallel to an intersection of two {111} planes. (b) The three slip planes that intersect the (111) surface. (c) The (110) surface and the four {111} planes that intersect it. Two {111} planes are inclined to the surface while two are normal to it. The two that are normal are each shown twice to illustrate how they combine to give an indentation like that of Fig. 4(c).

modulus of Au. This variation is greater than the theoretical results of Vlassak and Nix.[22] They calculated the expected indentation modulus of a rigid, flat, triangular indenter as a function of orientation for materials with different Poisson's ratios. The surface stress necessary to cause a given displacement was calculated for n points (n was varied from 64 to 3600), which involved the numerical solution of n simultaneous linear equations. Integrating the pressure distribution gave the total load, and from the load-displacement relationship the indentation modulus was predicted. The results for Au (assuming $\nu=0.45$) were that the (111) orientation has a 10% greater indentation modulus than the (001) (we measure 36%) and only a 2% greater value than (110) (we measure 3%). The primary difference between the situation modeled by Vlassak and Nix[22] and our indentations is that they consider a flat, rigid, triangular punch while we apply a Hertzian pressure distribution over a circular [or ellipsoidal for the (110) orientation] area. The stress distribution under the two types of indenters is quite different. Normal stresses tend to infinity at the edge of a flat punch indenter, while they tend to zero for Hertzian indentation.[18]

On the other hand, atomistic simulations of Kelchner and Hamilton,[20] which are simulations of Hertzian indentation, predict an effect of anisotropy on an indentation modulus that is greater than both the predictions of Vlassak and Nix and our observations. The difference in indentation

modulus between (111) and (001) orientations was approximately 50%, and that between (111) and (110) was approximately 20%.[20] These simulations use an 80 Å probe radius indented to depths of only ~5 Å, both of which are at least an order of magnitude smaller than those used in this study. However, all three studies are in agreement that the (111) orientation has the highest indentation modulus and the (001) the lowest; it is only over the magnitude of variation in which they differ.

Plastic threshold/indentation yield stress

In quantifying the yield point of Au as a function of orientation, we have measured the mean stress normal to the surface and have found that it varies considerably. Although this is the stress we can measure most accurately, plastic deformation is a result of shear stresses.[23] To arrive at a critical shear stress at which dislocations are activated, we must estimate the shear stresses beneath the indenter. A common approach to estimating the shear stress is to take the maximum value of the principal shear stress.[19] For a Hertzian stress distribution for a material with a Poisson's ratio of 0.3, the maximum shear stress occurs along the axis of symmetry at a depth of approximately $a/2$, where a is the radius of the contact area.[19] At this point, the shear stress is given by[18]

$$\tau = 0.465\bar{\sigma}, \tag{4}$$

where $\bar{\sigma}$ denotes the mean stress on the surface. This principal shear acts on planes inclined to the surface at 45°, but is not necessarily the stress that produces plastic deformation.

In fcc materials, slip occurs on close-packed {111} planes in ⟨110⟩ directions.[24] Therefore, we calculate the maximum resolved shear stresses on {111} planes in ⟨110⟩ directions for each of the orientations at the yield point. Schematic illustrations of how these {111} planes intersect the three surfaces are presented in Fig. 5. ⟨110⟩ slip directions are parallel to the intersections of these planes. To calculate shear stresses, we must begin with a three-dimensional stress distribution. The stress normal to the surface is given by the Hertzian pressure, but how radial and tangential stresses arise from this applied stress depends upon material properties. Rigorously, the stress distribution will be determined by the crystal orientation and the elastic constants of the lattice, and will be different for each orientation. For simplicity, we use the Hertzian distribution with Poisson's ratios that vary with orientation. Starting with the stress distribution in a given coordinate system, stresses in any other coordinate system may be straightforwardly predicted using the direction cosines for a rotation from one system to the other.[19] For example, we can define a Hertzian stress distribution in the (001) system that has stress components along the [100], [010], and [001] directions.[18] To resolve the shear stress on the (11 1) plane in the $[\bar{1}01]$ direction, a new set of axes is defined to be $x_1 = 1/\sqrt{6}[\bar{1}\,\bar{1}\,2]$, $x_2 = 1/\sqrt{2}[\bar{1}01]$, and $x_3 = 1/\sqrt{3}[1\,\bar{1}\,\bar{1}]$. The stress tensor in the (11 1) system is found from the (001)-system stress tensor and the direction cosines for rotation between the two systems. The stress component σ_{23} of the $(1\bar{1}\,1)$-system stress tensor is then the shear stress on the (11 1) plane in the $[\bar{1}01]$ direction.

TABLE III. Maximum shear stress resolved in the direction of primary slip for three orientations of Au. Shear stresses are given as fractions of the mean normal stress applied to the surface, and the depth at which the maximum occurs is given as a fraction of the radius of contact. Estimates of τ_c were obtained by multiplying the calculated maximum shear stress by measured $\bar{\sigma}_p$.

Orientation	Component	Max. shear stress	Depth	τ_c (GPa)
(001)	$(\bar{1}\bar{1}\,1)[\bar{1}01]$	$0.336\bar{\sigma}$	$0.54a$	1.8 ± 0.1
(111)	$(1\bar{1}\,1)[\bar{1}01]$	$0.228\bar{\sigma}$	$0.53a$	1.7 ± 0.1
(110)	$(1\bar{1}\,1)[\bar{1}01]$	$0.236\bar{\sigma}$	$0.0a$	1.8 ± 0.2
(110)	$(1\ 11)[101]$	$0.378\bar{\sigma}$	$0.49a$	2.9 ± 0.3

Since we can determine the {111} ⟨110⟩ shear stress for any given applied stress state, we can predict the maximum shear at the yield point for each of the orientations. On the axis of symmetry, the stresses in the indentation coordinate system are given as a function of depth, z, by the expressions[18]

$$\frac{\sigma_r}{\bar{\sigma}} = \frac{\sigma_\theta}{\bar{\sigma}} = \tfrac{3}{4}(1+z^2/a^2)^{-1} - \tfrac{3}{2}(1+\nu)\left(1 - \frac{z}{a}\tan^{-1}(a/z)\right) \tag{5}$$

and

$$\frac{\sigma_z}{\bar{\sigma}} = -\tfrac{3}{2}(1+z^2/a^2)^{-1}. \tag{6}$$

We have calculated {111} ⟨110⟩ shear stresses on the axis of symmetry from Eqs. (5) and (6) and have determined the maximum value and the position at which it occurs. The results are presented in Table III. Since the shear stress is given as a fraction of the mean applied stress, we can estimate the actual value of the maximum shear at the yield point (τ_c) from the measured applied mean stresses ($\bar{\sigma}_p$) listed in Table II.

The most striking result of these estimates is that τ_c is approximately equal on the (11 1) plane for each of the orientations, and the symmetry of {111} planes suggests stresses will be similar among slip planes for each orientation. For example, the (001) orientation has four symmetric slip planes, illustrated in Fig. 5(a), and τ_c is identical on all of them. The same is true of the three slip planes for the (111) orientation, illustrated in Fig. 5(b). τ_c is not identical on all slip planes for the (110) orientation, however. It is larger on the $(1\ \bar{1}1)$ plane [and, by symmetry, the (111) plane] than on the $(1\bar{1}\ 1)$ and (111) planes, and it occurs at a different depth. To understand how slip plane symmetry affects indentation, we will next develop a criterion for plastic indentation based on a critical shear stress for slip and the geometry of deformation.

Indentation yield point

Early work on single crystals showed that while there was a marked orientation dependence of the uniaxial yield strength, when the shear stress was resolved on the slip plane, a constant value was obtained for a given metal.[25] This constant value is referred to as the critical resolved shear stress (CRSS), and according to the Schmid law,[24,25] a

slip system can be activated when the resolved shear stress on that system reaches the CRSS. We can use this criterion to predict the activation of slip systems, but we must also consider the geometry of deformation. In the simplest case, a uniaxial tension test of a single crystal, the activation of a single slip system will provide the necessary extension and the yield criterion simply becomes the attainment of the CRSS.[25] The deformation resulting from an indentation experiment is considerably more complex, and the attainment of a CRSS on any one slip system does not necessarily produce general yield.[26] We propose that the criterion for creating an indentation is that the CRSS be attained on enough slip systems to give the plastic strains required by the indentation geometry.

Continuum treatments of plastic indentation model plastic strain as radial flow of material away from the indenter, similar to a plastically expanding hemispherical cavity.[27–29,18] When considered in Cartesian coordinates, this spherically symmetric flow of the indented half-space has components of plastic strain along all three coordinates. We will assume that our indentations have some component of plastic strain in three directions, and we will consider what slip systems must be activated for this type of strain. Active slip systems may be predicted by determining the resultant strain of a given slip system and the stress necessary to activate that system.[26] By considering the strains from all 12 slip systems, one may identify which systems contribute to the observed strain. Reid[30] (p. 174) has analyzed active slip systems necessary for plane strain compression as a function of orientation, the results of which are directly applicable. Compression in the [001] direction results in plastic strains in ⟨100⟩ directions and requires the activation of slip on the four {111} planes illustrated in Fig. 5(a). Likewise, compression along the [111] direction activates slip on the three {111} planes in Fig. 5(b) to give ⟨112⟩-type plastic strains. For the (110) orientation, plastic strain occurs in the [001] direction on the two planes inclined to the surface shown in Fig. 5(c). These are the two planes for which τ_c was estimated to be 2.9 GPa. However, for plastic strains in the [110] direction, slip on all four {111} planes must occur.

The conclusion of this analysis is that for the three orientations considered in this study, radial plastic strains, necessary in continuum indentation models, require slip on all {111} planes that are noncoplanar with the surface. These planes are illustrated in Fig. 5. Since slip is activated when the CRSS is attained, it follows that this CRSS must be attained on all such {111} planes to give an indentation. This model is consistent with our estimates of τ_c for the three crystal orientations (Table III), where we found that the yield point occurred once τ_c reached 1.8 GPa on all slip planes.

Although we have that observed τ_c is orientation-independent and have developed an indentation yield criterion based on this observation, the details of how applied stresses activate dislocation activity in nanoindentation experiments have not yet been fully developed. An earlier model of nanoindentation related yield points from probes with different tip radii to the nucleation of dislocation loops at a point directly beneath the indenter.[1] While we have neglected dislocation theory and have focused on crystallography, a combination of the two (i.e., nucleation of dislocation-loops on all {111} planes that intersect the surface) is likely a more accurate description of the slip process. The position of maximum τ_c may not be the site of loop nucleation. Atomistic simulations of the first two dislocation events indicate that dislocations originate at the surface,[20] not beneath the indenter on the axis of symmetry. Image force considerations also suggest that nucleation is more favorable at the surface.[31]

An important point to be noted is that we have not measured single dislocation events. The yield points we have quantified involve numerous dislocations on multiple slip systems. Typical probe displacements during these events involve ten atomic layers, which occur over the entire contact area (contact diameters were typically ≈ 600 Å). Also, the existence of shear stresses above the τ_c of 1.8 GPa on some slip systems for the (110) orientation (see above) indicates that some initial dislocation activity occurs before the detectable yield point. Exactly what type of dislocation activity occurs at the yield point is not clear, although it is likely that the activation of cross-slip is involved. The CRSS we have measured, then, describes a combination of events that together results in a permanent indentation and not necessarily the stress for nucleation of a single loop.

The high value of τ_c suggests that we are approaching the theoretical shear strength of the Au lattice. This is not true of macroscopic measurements of the yield strength, which involve the activation of preexisting dislocations and defects and occur at stresses that are on the order of 1 MPa.[32] Nanoindentation, on the other hand, concentrates stresses in a volume small enough that a defect is unlikely to be present. As an example, the radius of the volume under the indenter, which experiences a majority of the indentation stress, is on the order of 50 nm, while a typical mean dislocation spacing is on the order of 1 μm.[23] Without defects, plastic slip occurs when the ideal shear strength is attained, which can be modeled by considering the stress necessary to slip one section of the lattice past the adjoining section. Depending upon the potential used to model atomic interactions, estimates of the ideal shear strength of the Au lattice range from 0.74 to 10.9 GPa.[31] Our measurements are within this range, giving a clear indication that the properties of the ideal lattice are being measured.

Other measurements of the ideal shear strength of Au show good agreement with our measurements. Using Eq. (4) to estimate the shear stress, Michalske and Houston[1] found that $\tau_c \approx 3-4$ GPa. These values are reduced by half if the shear stress in the direction of slip is resolved, giving $\tau_c \approx 1.5-2$ GPa. Using a Berkovich indenter and Eq. (4), Corcoran *et al.*[8] found $\tau_c \approx 1.5$ GPa for the (111) orientation, but this surface was heavily defected. For (110) and (001) orientations, they found $\tau_c \approx 4$ GPa in the absence of surface defects, which is reduced to 1.3 GPa when the shear stress is resolved in the slip direction for the (001) orientation. Nanowire experiments[33,34] provide another test of ideal properties, since stressed volumes are too small for dislocations to exist. Stadler and Dürig[34] found that plastic deformation occurred when the applied normal stress reached 5–8 GPa, which is the same range of critical *normal* stresses that we found. Agraït *et al.*[35] measured the critical shear stress from nanowires and found that $\tau_c \approx 1.5$ GPa.

SUMMARY AND CONCLUSIONS

We have used the interfacial force microscope to quantify the variation of indentation modulus and initial plastic yield stress with crystal orientation. Au single crystals with (001), (111), and (110) orientations were passivated with a self-assembling monolayer and probed using a parabolic W tip. By referring experimental results to the (111) orientation, we found that the indentation modulus for the (111) orientation was 36% greater than for the (001) orientation and that there was no statistically significant difference between (111) and (110) orientations. We showed that the initial yield point also varied considerably with orientation. The mean applied stress necessary to initiate plasticity was 5.5 GPa for (001)-oriented crystals, 7.3 GPa for (111)-oriented crystals, and 7.8 GPa for (110)-oriented crystals. Assuming an isotropic Hertzian stress distribution, we have resolved maximum shear stresses on $\{111\}\langle 110\rangle$ slip systems for each of the orientations and, by combining these predictions with known applied stresses, we have estimated the shear stress on $\{111\}\langle 110\rangle$ slip systems at the initial yield point. The shear stress component on the $(11\,1)[101]$ slip system at the initial yield point was approximately 1.8 GPa for all three orientations. Using the simple yield criterion that the CRSS must be attained on enough slip planes to create an indentation, we have proposed that 1.8 GPa is the CRSS for creating a permanent indentation in Au. Since the processes by which dislocations nucleate, cross-slip, and interfere during the formation of an indentation are unknown, it is unclear what process or processes the measured CRSS quantifies. It is clear, however, that performing indentation experiments on the nanometer level can provide information on material properties that are not dominated by preexisting defects. It is also clear that these measurements, when considered in conjunction with theoretical modeling, can provide values for fundamental material parameters.

ACKNOWLEDGMENTS

This work was supported by the U.S. Department of Energy under Contract No. DE-AC04-94AL85000. Sandia is a multiprogram laboratory operated by Sandia Corporation, a Lockheed-Martin Company, for the U.S. Department of Energy.

[1] T. A. Michalske and J. E. Houston, Acta Mater. **46**, 391 (1998).
[2] P. Tangyunyong, R. C. Thomas, J. E. Houston, T. E. Michalske, R. M. Crooks, and A. J. Howard, Phys. Rev. Lett. **71**, 3319 (1993).
[3] P. Tangyunyong, R. C. Thomas, J. E. Houston, T. A. Michalske, R. M. Crooks, and A. J. Howard, J. Adhes. **8**, 897 (1994).
[4] R. C. Thomas, J. E. Houston, T. A. Michalske, and R. M. Crooks, Science **259**, 1883 (1993).
[5] J. B. Pethica and D. Tabor, Surf. Sci. **89**, 182 (1979).
[6] N. Gane and F. P. Bowden, J. Appl. Phys. **39**, 1432 (1968).
[7] N. Gane, Proc. R. Soc. London, Ser. A **317**, 367 (1970).
[8] S. G. Corcoran, R. J. Colton, E. T. Lilleodden, and W. W. Gerberich, Phys. Rev. B **55**, R160 57 (1997).
[9] W. W. Gerberich, J. C. Nelson, E. T. Lilleodden, P. Anderson, and J. T. Wyrobek, Acta Mater. **44**, 3585 (1996).
[10] S. Bec, A. Tonck, J.-M. Georges, E. Georges, and J. L. Loubet, Philos. Mag. A **74**, 1061 (1996).
[11] J. B. Pethica, R. Hutchinson, and W. C. Oliver, Philos. Mag. A **48**, 593 (1983).
[12] M. F. Doerner and W. D. Nix, J. Mater. Res. **1**, 601 (1986).
[13] S. A. Joyce and J. E. Houston, Rev. Sci. Instrum. **62**, 710 (1991).
[14] T. Hsu and J. M. Cowley, Ultramicroscopy **11**, 239 (1983).
[15] J. Schneir, R. Sonnenfeld, O. Marti, P. K. Hansma, J. E. Demuth, and R. J. Hamers, J. Appl. Phys. **63**, 717 (1988).
[16] J. E. Houston, T. A. Michalske, and R. M. Crooks, *Interfacial Adhesion at the Molecular Level*, in *20th Annual Meeting of the Adhesion Society, 1997* (The Adhesion Society, Hilton Head, SC, 1997).
[17] S. A. Joyce, R. C. Thomas, J. E. Houston, T. A. Michalske, and R. M. Crooks, Phys. Rev. Lett. **68**, 2790 (1992).
[18] K. L. Johnson, *Contact Mechanics* (Cambridge University Press, Cambridge, 1996).
[19] S. P. Timoshenko and J. N. Goodier, *Theory of Elasticity*, 3rd ed. (McGraw-Hill, New York, 1970).
[20] C. L. Kelchner and J. C. Hamilton, Phys. Rev. Lett. (to be published).
[21] R. W. Hertzberg, *Deformation and Fracture of Engineering Materials* (Wiley, New York, 1989).
[22] J. J. Vlassak and W. D. Nix, J. Mech. Phys. Solids **42**, 1223 (1994).
[23] D. Hull and D. J. Bacon, *Introduction to Dislocations*, 3rd ed. (Pergamon, Oxford, 1984).
[24] R. W. K. Honeycombe, *The Plastic Deformation of Metals* (St. Martin's Press, New York, 1968).
[25] E. Schmid and W. Boas, *Crystal Plasticity* (Hughes & Co. Ltd., London, 1950).
[26] G. W. Groves and A. Kelly, Philos. Mag. **8**, 877 (1963).
[27] R. F. Bishop, R. Hill, and N. F. Mott, Proc. Phys. Soc. London **57**, 147 (1945).
[28] D. M. Marsh, Proc. R. Soc. London, Ser. A **279**, 420 (1964).
[29] K. L. Johnson, J. Mech. Phys. Solids **18**, 115 (1970).
[30] C. N. Reid, *Deformation Geometry for Material Scientists* (Pergamon, Oxford, 1973).
[31] J. P. Hirth and J. Lothe, *Theory of Dislocations*, 2nd ed. (Wiley, New York, 1982).
[32] T. E. Mitchell, Prog. Appl. Mater. Res. **6**, 117 (1964).
[33] C. Untiedt, G. Rubio, S. Vieira, and N. Agraït, Phys. Rev. B **56**, 2154 (1997).
[34] A. Stalder and U. Dürig, Appl. Phys. Lett. **68**, 637 (1996).
[35] N. Agraït (private communication).